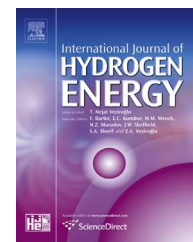


Available online at [www.sciencedirect.com](http://www.sciencedirect.com)

ScienceDirect

journal homepage: [www.elsevier.com/locate/ije](http://www.elsevier.com/locate/ije)

# Hydrogen embrittlement associated with strain localization in a precipitation-hardened Fe–Mn–Al–C light weight austenitic steel

Motomichi Koyama<sup>a,c,\*</sup>, Hauke Springer<sup>a</sup>, Sergiy V. Merzlikin<sup>a</sup>, Kaneaki Tsuzaki<sup>b,c</sup>, Eiji Akiyama<sup>b</sup>, Dierk Raabe<sup>a</sup>

<sup>a</sup> Max-Planck-Institut für Eisenforschung GmbH, Max-Planck-Straße 1, 40237 Düsseldorf, Germany

<sup>b</sup> National Institute for Materials Science, 1-2-1 Sengen, Tsukuba, Ibaraki 305-0047, Japan

<sup>c</sup> Department of Mechanical Engineering, Kyushu University, 744 Motoooka, Nishi-ku, Fukuoka 819-0395, Japan

## ARTICLE INFO

### Article history:

Received 6 September 2013

Received in revised form

21 December 2013

Accepted 27 December 2013

Available online 27 January 2014

### Keywords:

Austenitic steel

Precipitation hardening

Hydrogen embrittlement

Tension test

Electron channeling contrast imaging

## ABSTRACT

Hydrogen embrittlement of a precipitation-hardened Fe–26Mn–11Al–1.2C (wt.%) austenitic steel was examined by tensile testing under hydrogen charging and thermal desorption analysis. While the high strength of the alloy (>1 GPa) was not affected, hydrogen charging reduced the engineering tensile elongation from 44 to only 5%. Hydrogen-assisted cracking mechanisms were studied via the joint use of electron backscatter diffraction analysis and orientation-optimized electron channeling contrast imaging. The observed embrittlement was mainly due to two mechanisms, namely, grain boundary triple junction cracking and slip-localization-induced intergranular cracking along micro-voids formed on grain boundaries. Grain boundary triple junction cracking occurs preferentially, while the microscopically ductile slip-localization-induced intergranular cracking assists crack growth during plastic deformation resulting in macroscopic brittle fracture appearance.

Copyright © 2014, Hydrogen Energy Publications, LLC. Published by Elsevier Ltd. All rights reserved.

## 1. Introduction

Among the different microstructural concepts suited for designing high strength structural steels, stable austenite appears favorable for hydrogen-related infrastructure (i.e. storage, transportation, energy conversion) due to its lower susceptibility for hydrogen embrittlement in comparison to ferrite [1], martensite [2] or metastable austenite (i.e. which transforms to martensite when exposed to mechanical loads) [3]. In more recent steel alloy design concepts the austenite is

stabilized by high amounts of manganese (Mn) and carbon (C), and as a result a desirable combination of high tensile strength up to 1 GPa with a large uniform elongation of 60% or higher can be achieved [4–6]. Most of these austenitic alloys show high tensile elongations owing to mechanical twinning and complex cell structure formation [6–8]. One of the main factors enhancing the mechanical properties of these ‘twinning-induced plasticity (TWIP)’ steels is the high work hardening capacities resulting from deformation twinning and the associated dislocation plasticity [6–8]. This attractive combination of mechanical properties is utilized not only in steel

\* Corresponding author. Department of Mechanical Engineering, Kyushu University, 744 Motoooka, Nishi-ku, Fukuoka 819-0395, Japan.

E-mail address: [koyama@mech.kyushu-u.ac.jp](mailto:koyama@mech.kyushu-u.ac.jp) (M. Koyama).

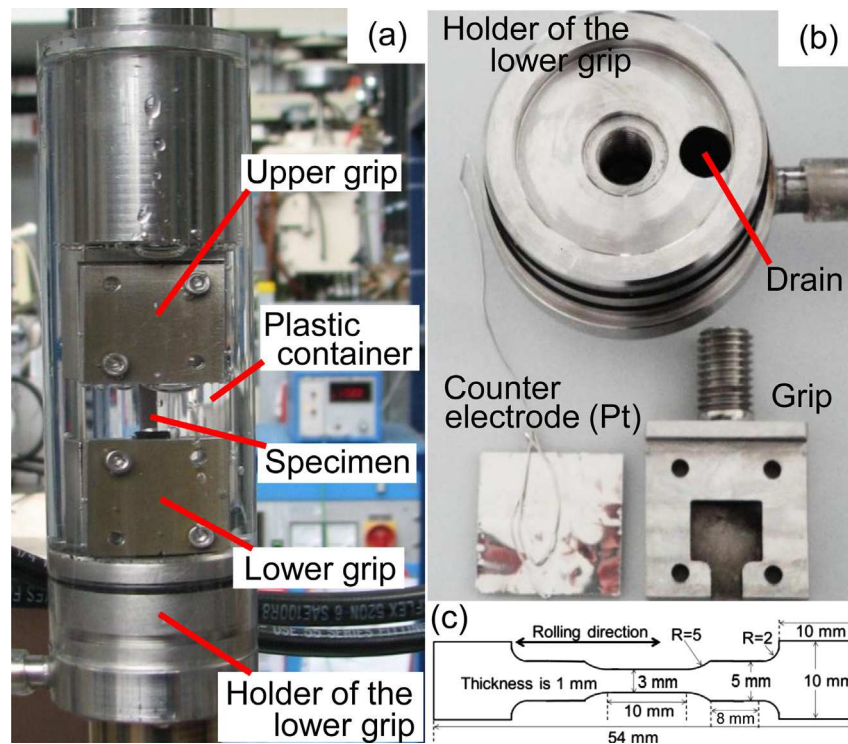


**Fig. 1 – (a) A setup for the tensile testing under hydrogen charging. (b) The parts of the setup. (c) The geometry of tensile specimens.**

applications for hydrogen-related infrastructures, but also in potentially highly mechanically loaded automotive components for reasons of weight reduction [9,10].

The addition of aluminum to such Fe–Mn–C-based alloys increased the materials strength even further, while strongly reducing the specific weight [11,12]. Since Al and C promote formation of ferrite and carbide, respectively, Al-containing TWIP steels can consist of three phases, depending on heat treatment [11,12], and hence are also referred to as ‘TRIPLEX’ steels. Austenite serves the majority phase, while ferrite and Al-based  $\kappa$ -carbide ( $\text{Fe,Mn}_3\text{AlC}$  [13] are minority phases [11]. The increase in Al content and ferrite fraction decreases the mass density due to the smaller atomic weight of Al compared to Fe as well as the difference in atomic density between the fcc and bcc structures in steels [11]. The yield strength of Mn–C–Al steels can be enhanced by precipitation hardening through the formation of  $\kappa$ -carbide [11,12,14]. In addition, the formation of  $\kappa$ -carbide plays a key role on the reported strong slip localization during deformation, providing superior uniform elongation [11,14–16]. However, as hydrogen embrittlement occurs preferably in strain-localized regions, this slip-localization trend observed in TRIPLEX steels is speculated to have an influence on hydrogen embrittlement, which is of high importance for using in hydrogen-related infrastructures such as a hydrogen storage tanks [17,18].

Several publications have presented investigations on hydrogen embrittlement of Mn–C-based high strength steels [19–23]. A Fe–18Mn–1.2C TWIP steel was reported to show intergranular cracking as well as twin boundary cracking [19,20]. While ferrite/austenite boundary cracking and slip-localization-related cracking were observed in a Mn–C–Al

alloyed steel [17], a comprehensive understanding of the respective hydrogen embrittlement mechanisms and their interactions are still impeded by the microstructural complexity of these materials. Thus, in this study, we focus on hydrogen effects on tensile properties and hydrogen-assisted cracking mechanism in an austenitic Mn–C–Al steel (without ferrite phase), to investigate the role of strain localization phenomena associated with the occurrence of  $\kappa$ -carbide precipitations in an austenitic matrix with a high stacking fault energy.

In previous studies [19,20], we introduced the joint use of electron backscatter diffraction (EBSD) and electron channeling contrast imaging (ECCI) analyses for studying hydrogen-related cracks in a Fe–Mn–C austenitic steel. The microstructure observations in the vicinity of the crack enabled us to establish direct correlations between microstructure and cracking mechanism such as crack initiation site and propagation path. Since the present steel used for this study is also austenitic, we employ the same experimental approach.

## 2. Experimental procedure

The Fe-25.7Mn–10.6Al–1.16C (wt.%) alloy is a  $\kappa$ -carbide-hardened austenitic steel [11]. It was prepared by induction melting under argon atmosphere and cast into a copper mold. After homogenization under air at 1150 °C for 2 h, the ingot was hot rolled at a starting temperature of 1050 °C from 60 mm down to a hot strip of 2.5 mm in thickness. Then it was solution treated at 1050 °C for 25 min and subsequently water quenched. The average grain size was 32  $\mu\text{m}$  including the annealing twin boundaries.

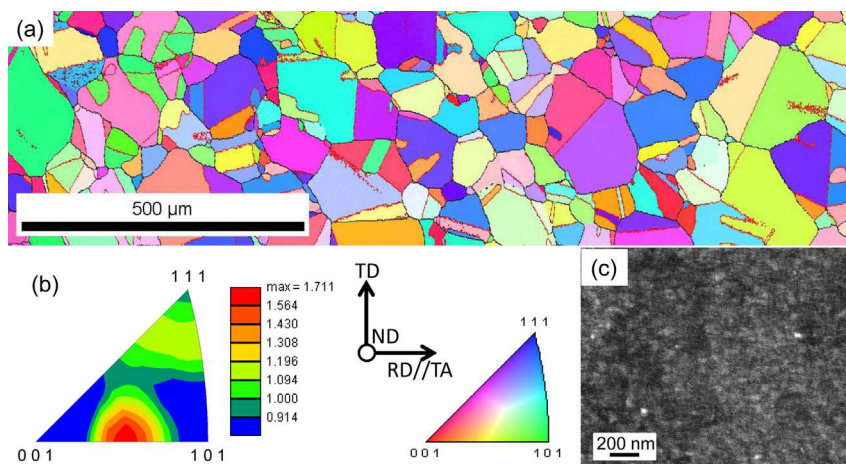


**Fig. 2 – Initial microstructures of the as-solution treated specimen. (a) RD-IPF EBSD map. The black and red lines indicate high angle and  $\Sigma 3$  twin boundaries, respectively. (b) Orientation distribution along RD obtained from (a). (c) Orientation-optimized ECC image showing nm-sized precipitates (RD: rolling/longitudinal direction; IPF: inverse pole figure). (For interpretation of the references to color in this figure legend, the reader is referred to the web version of this article.)**

Tensile testing was conducted at room temperature with an initial strain rate of  $10^{-4} \text{ s}^{-1}$  (cross head speed) along the rolling direction (RD) using a hydraulic testing machine, Instron 8511. The tensile specimens with gage dimensions of 3 mm wide  $\times$  1 mm thick  $\times$  10 mm long shown in Fig. 1c were cut by spark erosion. Three tests each were conducted at air and under hydrogen charging (Fig. 1a and b). The gage part was exposed to the solution and charged with hydrogen. The other immersed parts of the specimen, the grips, and metallic constituents of the cell in the solution were covered with a non-conductive lacquer spray. Hydrogen was introduced into the specimens before the tensile test for 40 min and also continuously during the tensile tests by electrochemical charging in a 3% NaCl aqueous solution containing 3 g/L of  $\text{NH}_4\text{SCN}$  at a cathodic current density of  $10 \text{ A m}^{-2}$ . A platinum foil with dimensions of 25 mm wide  $\times$  0.1 mm thick  $\times$  25 mm long was used as the counter electrode. Since the surface area of the Pt foil in the solution was  $1260 \text{ mm}^2$ , the anodic current density was about  $0.8 \text{ A m}^{-2}$ . Hydrogen charging was stopped when the specimen failed. Hence, the total hydrogen charging time is determined by the pre-charging time (40 min) and fracture strain divided by the strain rate. Hydrogen charging during tensile testing introduced hydrogen effectively into the samples via diffusion as well as through the motion of hydrogen-decorated dislocations [24,25]. It was observed before that such tensile tests conducted directly under hydrogen charging revealed hydrogen embrittlement of fully austenitic high strength Fe–Mn–C TWIP steels [22,26,27]. Hydrogen uptake before the start of the tensile test was measured by thermal desorption analysis (TDA) from room temperature to  $900 \text{ }^\circ\text{C}$  using a quadrupole mass spectrometer for detection of the gases. The specimen used for TDA was charged with hydrogen in the same solution as that used for the tensile test (40 min prior to deformation) at a current density of  $10 \text{ A m}^{-2}$ .

TDA was started within 25 min after the tensile test. The heating rate was changed from  $6.5$  to  $26 \text{ }^\circ\text{C min}^{-1}$  to estimate the spectrum of activation energies for hydrogen desorption pertaining to a specific trap site distribution. The activation

energies were estimated by using a Kissinger plot as defined in Ref. [28], i.e.

$$\frac{\partial \ln\left(\frac{\varphi}{T_c^2}\right)}{\partial\left(\frac{1}{T_c}\right)} = -\frac{E_a}{R} \quad (1)$$

where  $\varphi$  is heating rate,  $T_c$  the temperature at which the maximum of the hydrogen desorption peak occurs,  $R$  the gas constant, and  $E_a$  the activation energy for hydrogen desorption. The activation energies for hydrogen desorption from the different trap sites are calculated as the slope of a  $\ln(\varphi/T_c^2)$  vs  $1/T_c$  plot. The obtained activation energies are then used to identify the active hydrogen trap sites.

Microstructure observations were performed in the scanning electron microscope (SEM) by secondary electron imaging (SEI), electron backscatter diffraction (EBSD), and ECCI. The specimens were prepared by standard mechanical polishing techniques. For SE and ECC imaging the SEMs were operated at 15 kV accelerating voltage. The EBSD analysis was operated at 20 kV with a beam step size of 300 nm or 1  $\mu\text{m}$ , respectively. The microstructure observations were conducted 10 days or longer after conducting the in-situ hydrogen-charged tensile tests. Since diffusible hydrogen in a Fe–Mn–C austenitic steel was reported to be completely desorbed after exposure to air for 10 days [29], the diffusible hydrogen content of the present specimen was assumed to be negligibly low when the microstructure was observed.

### 3. Results

#### 3.1. Undeformed microstructures and hydrogen uptake affecting the tensile properties

Fig. 2a shows the rolling direction (RD)-inverse pole figure (IPF) map of the as-solution-treated specimen. The RD-IPF EBSD map indicates that the initial microstructure is austenite

without ferrite, and includes  $\Sigma 3$  annealing twin boundaries. The crystallographic orientation along RD is randomly distributed with a small peak near  $\langle 102 \rangle$  as shown in Fig. 2b. Fig. 2c shows an orientation-optimized ECC image which shows nano-sized precipitates. Since the orientation of the grain is optimized for Bragg's condition in Fig. 2c, the matrix is imaged as black, and the precipitate appear in relatively bright contrast. When the orientation is rotated to realize optimized Bragg contrast, the grain appears dark on the ECC image because of the low back scattering yield [30]. Dislocations, twins, and second phases such as precipitates locally affect the channeling contrast, and hence are revealed with a bright contrast.

Fig. 3 shows engineering stress–strain curves of the specimens with and without hydrogen charging. The flow stress slightly decreased at low plastic strains, and sustained or increased at higher strains. This characteristic behavior is identical to previously reported stress–strain responses of TRIPLEX steels with a similar composition [11]. The obtained tensile properties are summarized in Table 1. Although the yield strength did not change significantly, the elongation was deteriorated dramatically by hydrogen charging. The presence of hydrogen reduces the flow stress directly after the onset of yielding, leading to premature failure.

Fig. 4a–c shows hydrogen desorption rates plotted against temperature measured at different heating rates. These results were obtained in the specimens hydrogen-charged for 40 min without any plastic deformation. Hence, the hydrogen distribution and content correspond to those in the samples just before starting the tensile tests. Four peaks appeared in all of the three hydrogen desorption rate curves. In all cases the positions of the peaks shifted to higher temperatures with increasing heating rate. Since the first peak is separated clearly from the other peaks, the cumulative hydrogen content from room temperature to the finishing temperature of the first peak could be obtained as shown in Table 2. The

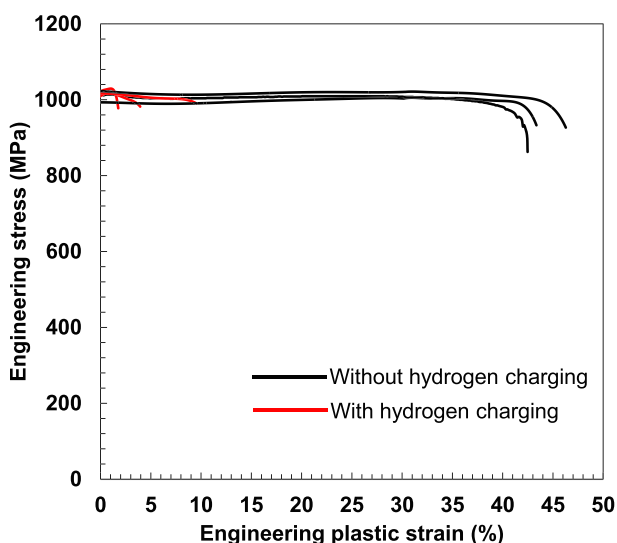


Fig. 3 – Engineering stress–strain curves with and without hydrogen charging. The hydrogen was introduced by hydrogen pre-charging for 40 min as well as in-situ hydrogen charging during the tests.

Table 1 – Tensile mechanical properties. PS: Proof Stress. UTS: Ultimate Tensile Strength.

	0.2% PS (MPa)	UTS (MPa)	Total elongation (%)
Without H	1009 ± 15	1012 ± 10	44 ± 2
With H	1015 ± 9	1018 ± 13	5 ± 4

average cumulative hydrogen content related to peak 1 is  $0.14 \pm 0.05$  mass ppm. Fig. 4d–g shows the Kissinger plots obtained from Fig. 4a–c. The activation energies for hydrogen desorption corresponding to peaks 1, 2, and 4 were found to be 27, 76, and 80  $\text{kJ mol}^{-1}$ , respectively. The activation energy for peak 3 was estimated to be around 78  $\text{kJ mol}^{-1}$ . Its determination was less precise compared to the three other peaks owing to the scatter in the corresponding Kissinger plot.

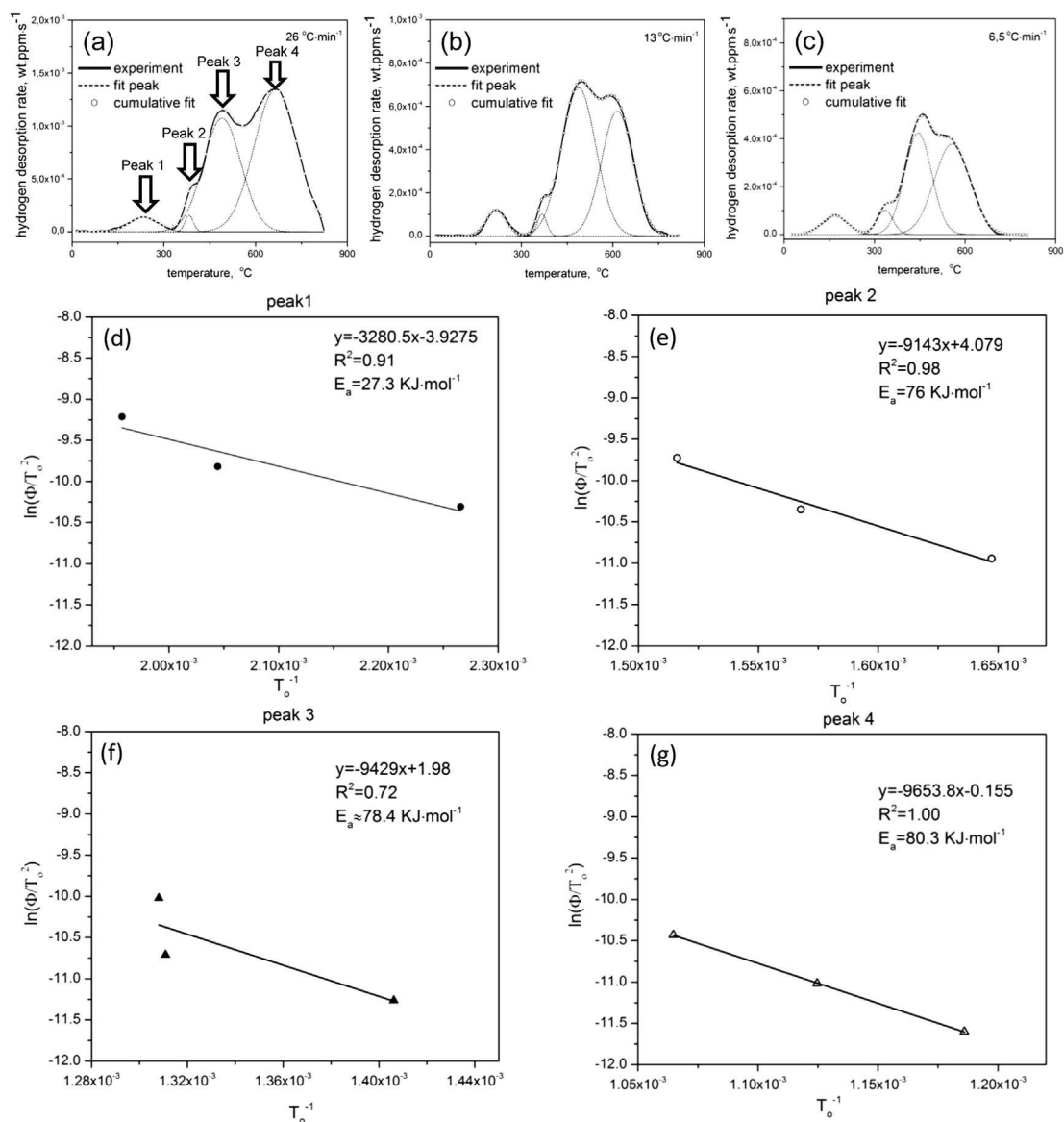
### 3.2. Deformation microstructure without hydrogen effect

Fig. 5 shows a set of micrographs obtained in the specimen fractured without hydrogen charging. Fig. 5a shows a low magnification ECC image at 5% plastic strain around which the fracture took place in the corresponding hydrogen-charged specimens shown in Fig. 3. The image indicates that 5% straining did not induce any martensite or deformation twins which should otherwise have appeared in the ECC image. The orientation-optimized ECC image at 5% plastic strain shown in Fig. 5b shows the grain matrix in dark contrast and localized slip in white contrast as indicated by arrows. In particular, strain localization shown in white contrast is remarkably intense at the intersections between such localized slip bands and the grain boundary as indicated by red arrows in Fig. 5c.

Fig. 5d shows a RD-IPF map with the corresponding IQ map taken in the vicinity of the necking region after the specimen had failed without hydrogen charging. The tensile texture is characterized by pronounced  $\langle 111 \rangle$  or  $\langle 001 \rangle$  orientations parallel to the tensile axis. Martensite as well as deformation twins were not observed. As indicated by the red arrow, only deformation bands without any phase and large (twin-like) orientation changes were observed in the IQ map. Hence these local plastic inhomogeneities are due to localized slip such as shown in Fig. 5b. In addition, cracking was observed along or in the vicinity of grain boundaries as indicated by the black arrows in Fig. 5d. Fractographs were also taken in the same specimen. The fracture surface was dominantly ductile as shown in Fig. 5e. However, some parts on the fracture surface showed specific ductile features in the form of surface steps as indicated by the dotted lines in Fig. 5f.

### 3.3. Hydrogen-assisted cracking and fracture

Fig. 6 shows a region of the fracture surface obtained in the specimen fractured with hydrogen charging (2% total elongation to fracture). Fig. 6a shows an overview image of the fracture surface. In the central region, the surface is dominated by dimples. In contrast, the fracture surface regions which are close to the side edges reveal characteristics of



**Fig. 4** – TDA results obtained at heating rates of (a) 26 °C min<sup>-1</sup>, (b) 13 °C min<sup>-1</sup>, and (c) 6.5 °C min<sup>-1</sup>. Kissinger plots showing the activation energies corresponding to (d) peak 1, (e) peak 2, (f) peak 3, and (g) peak 4 which are shown in (a–c).

intergranular cracking. Fig. 6b shows the magnified image of the right hand portion of Fig. 6a where intergranular fracture features prevail. The region highlighted by the square in Fig. 6b was further magnified as shown in Fig. 6c. In the vicinity of the specimen edge that is surrounded by the yellow dotted and white solid lines, a smooth intergranular fracture surface appears. On the other hand, the interior region relative to the yellow dotted line shows slip traces on the intergranular fracture surface, e.g. the region highlighted by the red dotted lines in Fig. 6c. The highlighted region is magnified

in Fig. 6d, revealing the multiple slip traces. In addition, intergranular cracking and ductile fracture features exist along the grain boundaries on the fracture surface as indicated by the black arrow and the circle in Fig. 6d, respectively.

Fig. 7a shows a cross sectional SE image taken on a specimen strained to 2% in the vicinity of the hydrogen-assisted fractured region after grinding about 300 μm from the surface. Several cracks were observed as indicated by the arrows. Fig. 7b shows hydrogen-assisted cracking at a grain boundary triple junction. Fig. 7c shows the corresponding Kernel

**Table 2** – Cumulative hydrogen contents corresponding to the first peak.

Heating rate (°C min <sup>-1</sup> )	Peak position (°C)	Peak center temperature (°C)	Hydrogen concentration (w. ppm)
6.5	RT-260	168	0.16
13	RT-300	218	0.18
26	RT-320	238	0.08

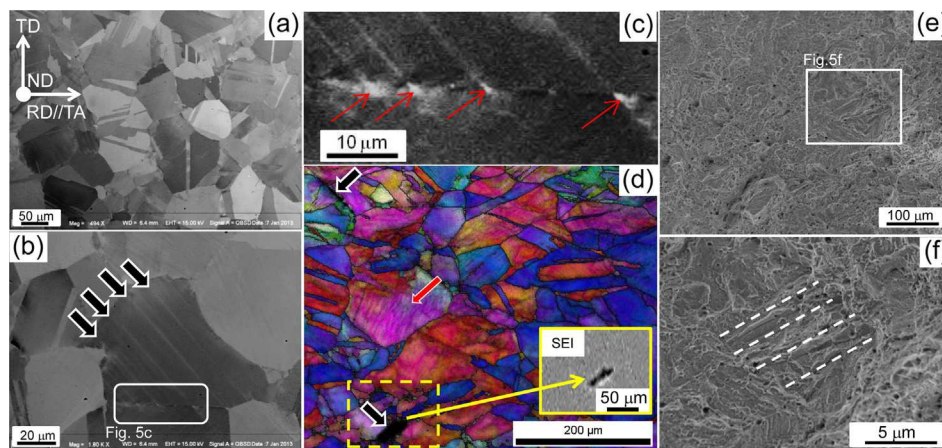


**Fig. 5 – Deformation microstructures without hydrogen charging.** TA: Tensile axis. (a) ECG image with 5% strain, and (b) its magnified image which is orientation-optimized. (c) The magnified image of (b) with an enhanced contrast. (d) RD-IPF + IQ map of the fractured specimen. The secondary electron image (SEI) was shown to evidence the occurrence of cracking. (e) Fracture surface of the specimen without hydrogen charging. (f) Magnified image of the part surrounded by dotted lines in (d) (RD: rolling/longitudinal direction; IPF: inverse pole figure; IQ: image quality).

average misorientation map (KAM). Local plastic straining is observed around the crack tips (indicated by the red arrows) as well as at the grain boundary triple junction (indicated by the black arrows). The Kernel average misorientation has been suggested as a measure of the geometrically necessary dislocation density [31] (see Fig. 7c). From that we observe that the amount of local plastic strain around the grain boundary triple junctions is comparable to that around the crack tips.

Fig. 8a shows a RD-IPF map of the grains surrounding the well-developed crack shown in Fig. 7a. The RD-IPF map indicates that the hydrogen-assisted cracking occurs preferentially along grain boundaries, which matches the observation of intergranular fracture shown in Fig. 6. The KAM map corresponding to Fig. 8a is shown in Fig. 8b to reveal locations where specifically high plastic strain localization and hence local lattice curvature occurs. Remarkable plastic strain localization takes place around the region outlined by the dotted lines. A more detailed microstructure analysis from the region with higher strain-localized was conducted using the orientation-optimized ECCI technique, Fig. 8c. Similar to the case without hydrogen charging, slip localization was observed particularly at the intersections of grain boundaries and slip bands. Also, voids along the grain boundaries were observed as indicated by the arrows.

In order to investigate the origin and development of the two hydrogen-related fracture modes observed (triple junction cracking and strain-localization-related intergranular cracking) in more detail, interrupted tensile testing was performed. First, the specimen was hydrogen-pre-charged for 40 min followed by deformation under hydrogen charging until the yield point. After unloading, the specimen was heated outside the tensile machine to 200 °C for 40 min in order to remove diffusible hydrogen. Then, the specimen was re-mounted and tensile tested without hydrogen charging until fracture. As can be seen from the engineering stress/strain curves shown in Fig. 9, the pre-deformation with hydrogen charging did not affect the tensile elongation and increased the work hardening slightly. However, the

corresponding fracture surface shown in Fig. 10a and b is not entirely ductile. Grain boundary triple junction cracking was observed at the vicinity of the specimen surface, although the fracture surface was covered dominantly by dimples. Also note that the surface of the cracks at the grain boundary triple junction is covered with small dimples (Fig. 10b).

## 4. Discussion

### 4.1. Microstructure characteristics without hydrogen

The undeformed microstructure of the investigated Mn–Al–C steel consists of austenite and precipitates (see Fig. 2). The nano-size precipitates in the investigated alloy system are well known to have a  $L1_2$  structures, namely, so-called  $\kappa$ -carbide [11,14,15]. Since  $\kappa$ -carbide is most probably formed through spinodal decomposition occurring already during quenching [32–34], it may be present even in the as solution-treated microstructure [11]. The formation of  $\kappa$ -carbide acts as an important strengthening factor [11,14,15], providing the high yield strength of the present steel as shown in Fig. 3.  $\epsilon$  (hcp)-martensitic transformation or deformation twinning was not observed in our experiments (Fig. 5a and d), unlike found in other Fe–Mn–C-based high strength austenitic steels [6,8,10]. This is related to the increased stacking fault energy of the investigated steel (reportedly about 110 mJ/m<sup>2</sup> [11]) compared to TWIP and hcp-martensite transformation-induced plasticity steels (0–40 mJ/m<sup>2</sup> [9,8,10]). Instead, slip localization was observed in our study (Fig. 5b). The occurrence of slip localization was shown to be caused by an enhancement of dislocation planarity arising from shearing of  $\kappa$ -carbide [14,15], and it is considered to assist micro-void formation in the intersections of grain boundary and localized slip band, causing the partial intergranular fracture shown in Fig. 5d. Hence, we conclude that the steps observed on the fracture surface in Fig. 5f result from slip-localization-assisted intergranular cracking.

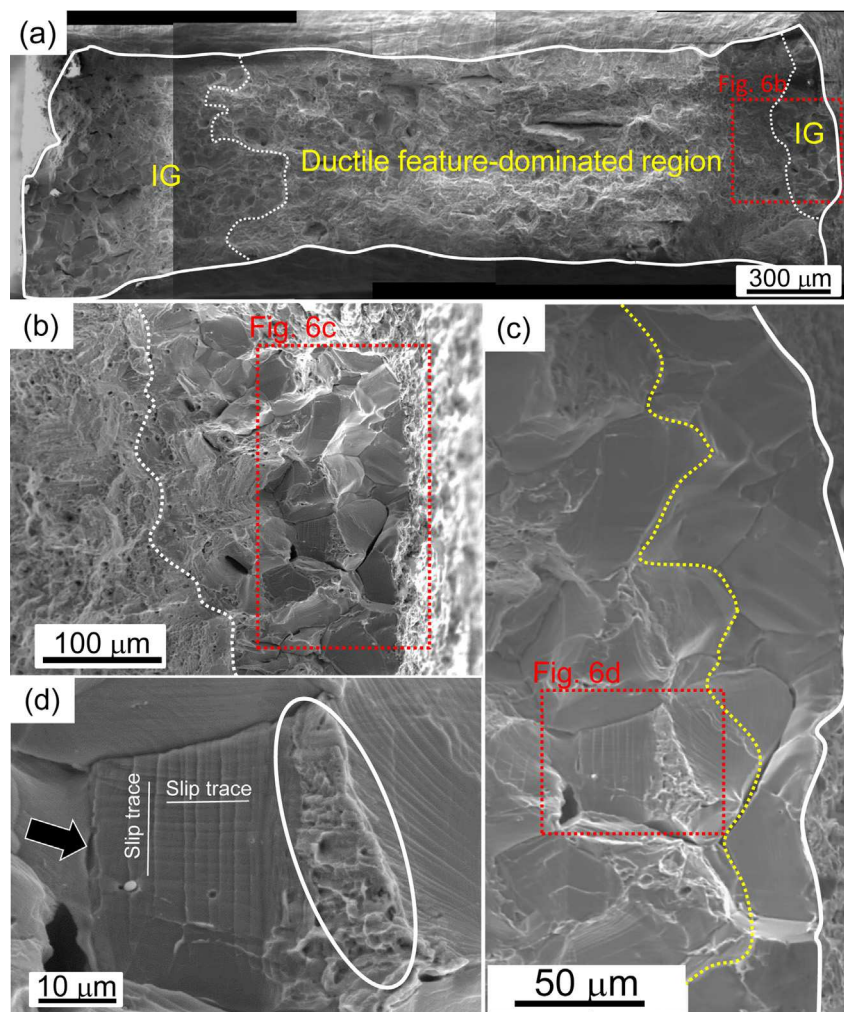


**Fig. 6** – Fractographs of the specimen deformed under hydrogen charging. (a) Entire image of the fracture surface. Magnified images of the parts surrounded by the red dotted lines in (b) Fig. 6a, (c) Fig. 6b, and (d) Fig. 6c. The white solid lines indicate the edges of the surface. The dotted white lines in (a) and (b) indicate the boundaries between intergranular fractured region (IG) and ductile feature-dominated region. The yellow dotted line in (c) indicates the boundary between the brittle surface with and without slip traces such as the ones shown in (d).

#### 4.2. Hydrogen uptake and embrittlement

Four peaks were observed in the hydrogen desorption curves shown in Fig. 4a–c. Their position and magnitude are discussed based on corresponding literature data for activation energies of hydrogen desorption from various hydrogen trap sites (Table 3). The activation energy pertaining to the first peak ( $27 \text{ kJ mol}^{-1}$ ) fits roughly to the data reported for hydrogen desorption from dislocations [28,35]. More specifically, the hydrogen desorption associated with the first peak is mainly attributed to capturing of hydrogen within the elastic field of an edge dislocation [42]. Since the dislocation density in the as-solution-treated specimens is low, the area under the first peak is much smaller than those under the third and fourth peaks, respectively. Also we assume that the first peak contained hydrogen which was desorbed from other low-barrier sites such as interstitial sites, vacancies, and grain boundaries. The hydrogen trapped in these sites has higher mobility compared to hydrogen stored at

dislocations, since the activation energies of hydrogen desorption from these sites are lower than that for hydrogen stored at the elastic field of edge dislocations [28,42]. The amount of diffusible hydrogen included also in the first peak can hence not be ignored, since the investigated steels contain grain boundaries, vacancies and other low-barrier capture sites. For example, in pure Ni as well as in an austenitic steel, hydrogen localization at grain boundaries [43] was revealed by secondary ion mass spectroscopy [44,45] and the silver decoration technique [46,47]. The contribution of these hydrogen trap sites can, however, not be distinguished by the TDA technique [39].

Peaks 2 and 4 exhibit activation energies for hydrogen desorption of  $76$  and  $80 \text{ kJ mol}^{-1}$ , respectively, which are much higher than that associated with peak 1. As shown in Table 3, only hydrogen desorption from precipitates can explain such high activation energies. In addition, the areas underneath peaks 2 and 4 are comparable or even higher compared to that of peak 1, indicating that the amount of hydrogen trapped at

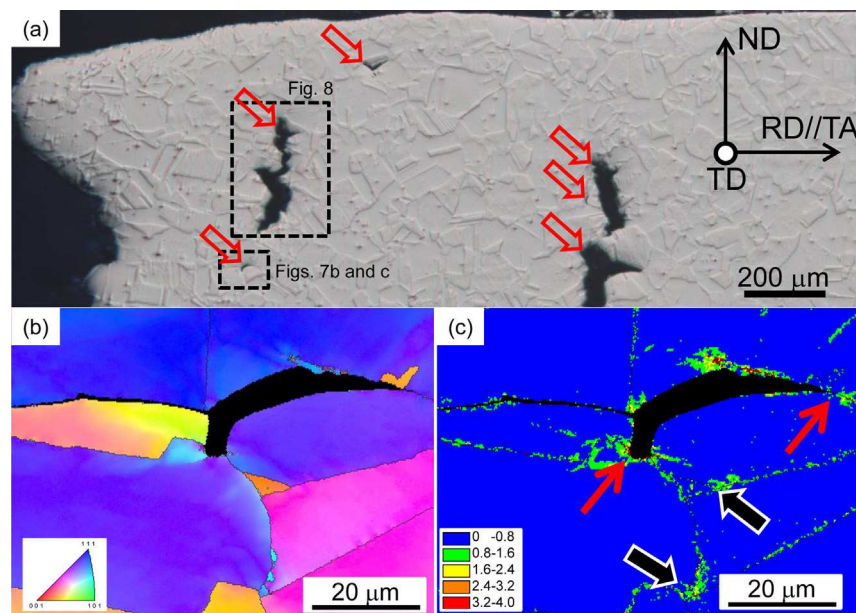


**Fig. 7 – Hydrogen-related sub cracks observed by SEM. (a) SE image. (b) RD-IPF maps and (c) the corresponding KAM values around the hydrogen-related crack at the grain boundary triple junction. The KAM values were calculated using first neighboring EBSD points at a distance of 300 nm (RD: rolling/longitudinal direction; IPF: inverse pole figure).**

precipitates (associated with peaks 2 and 4) must be significant compared to the amount of hydrogen captured of dislocations, vacancies etc. As  $\kappa$ -carbides are the only precipitates present in the investigated steel, we conclude that peaks 2 and 4 correspond to  $\kappa$ -carbide-related hydrogen desorption.

Peak 3 did not show a clear linear relation in the Kissinger plot (see Fig. 4f). This is explained by the gradual further formation and growth of  $\kappa$ -carbides during TDA heating (about 550 °C), as this temperature, corresponding to the position of peak 3, is a typical aging temperature to obtain  $\kappa$ -carbide [11,15]. It was reported that  $\kappa$ -carbide can significantly grow even within only 2 min at 550 °C [11]. The change in the stored hydrogen amount at  $\kappa$ -carbides, the motion of the  $\kappa$ -carbide/austenite boundaries due to carbide growth, and possibly also the variation of the elastic strain field around  $\kappa$ -carbides during heating of the TDA may shift the position of peak 3, depending on the heating rate. The influence in heat treatment conditions has been reported to change the activation energy for hydrogen desorption from precipitates [39,40]. Hence, we conclude that three of the peaks (2, 3, and 4) are caused by hydrogen desorption from  $\kappa$ -carbides, however, from  $\kappa$ -carbides with different elastic strain fields. In terms of coherency of  $\kappa$ -carbides, the elastic strain field changes with increased number of misfit dislocation [36,37] (see Fig. 11). The introduction of misfit dislocations accommodates the elastic misfit on carbide/matrix interface. Also, the misfit dislocations provide an elastic strain field around themselves. These facts change elastic strain field around  $\kappa$ -carbides, resulting in different coherencies. The difference in coherency would be a reason why the three different activation energies for hydrogen desorption can originate from  $\kappa$ -carbides.

The activation energies which are higher than 70 kJ mol<sup>-1</sup> corresponding to peaks 2 and 4, respectively, indicate that the desorbed hydrogen in these cases was irreversibly [36,37] or strongly trapped [48]. Peak 3 is also considered to be

irreversible, because the peak position appeared at a higher temperature compared to that for peak 2, and because the activation energy for hydrogen desorption associated with peak 3 was roughly 78 kJ mol<sup>-1</sup>. These facts indicate that  $\kappa$ -carbide acts as an irreversible hydrogen trap site, since peaks 2, 3, and 4 are associated with  $\kappa$ -carbide as discussed above. In contrast, the hydrogen which is desorbed with an activation energy of only 27 kJ mol<sup>-1</sup> (peak 1) is attributed to diffusible hydrogen [36]. This conclusion suggests that the diffusible hydrogen content, which dominates embrittlement [49], is determined as the amount of desorbed hydrogen in peak 1 as shown in Table 1.

#### 4.3. Mechanisms of hydrogen-assisted fracture

Hydrogen-assisted cracking was observed to take place mainly along grain boundaries. Typically, two types of hydrogen-assisted intergranular fracture were found in the investigated steel, namely, grain boundary triple junction cracking (Fig. 7b–c) and slip-localization-induced void formation and coalescence along grain boundaries (Fig. 8). Both effects together apparently cause the observed embrittlement.

Grain boundary triple junction cracking was observed also in nickel [50] as well as in Fe–Mn–C TWIP steel [19]. The mechanism was explained in terms of plastic strain localization due to the formation of deformation bands around grain boundary triple junctions [50]. This effect was assumed to promote hydrogen localization around grain boundary triple junctions, assisting brittle cracking through a reduction in the cohesive energy at grain boundaries. Additionally, the elastic misfit is also largest at the grain boundary triple junction, assisting cracking already at an early deformation stage. We observed a similar phenomenon in the current investigations (Fig. 7c). Hence, we suggest that plastic strain localization and

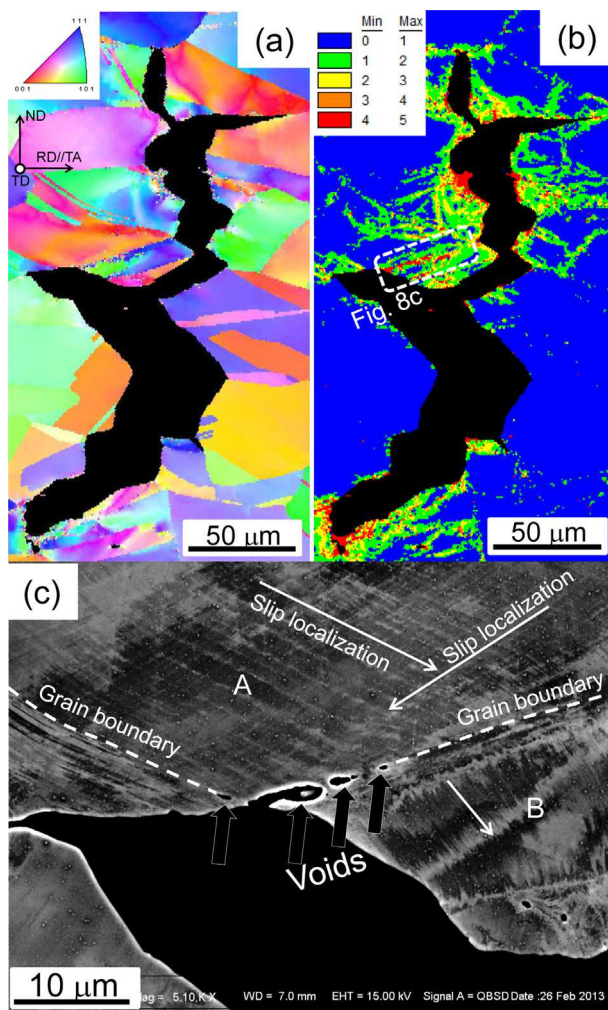


**Fig. 8 – (a) RD-IPF map. (b) KAM map. (c) Orientation-optimized ECC image corresponding to the part surrounded by the white broken lines in (b). The KAM values were calculated using first neighboring EBSD points at a distance of 300 nm (RD: rolling/longitudinal direction; IPF: inverse pole figure).**

elastic misfit cause the observed grain boundary triple junction cracking. Moreover, the plastic strain localization induces the dimples on the cracks at grain boundary triple junctions observed in the interrupted test (Fig. 10b).

The interrupted testing (Fig. 9) limited the effects of hydrogen to the elastic regime or to a strain level just after the onset of plastic yielding, since the diffusible hydrogen was desorbed by heating at 200 °C after interrupting the test (see Fig. 4c). This indicates that the nevertheless observed hydrogen-assisted grain boundary triple junction cracking (Fig. 10) in this state is initiated already in the elastic regime or during a regime below 1% plastic straining. Thus, grain boundary triple junction cracking is considered to be the first step in the hydrogen-assisted cracking phenomenon. This means that the grain boundary triple junction cracking caused the intergranular fracture surface without slip traces as observed in the vicinity of the sample surface (see Fig. 6c). In

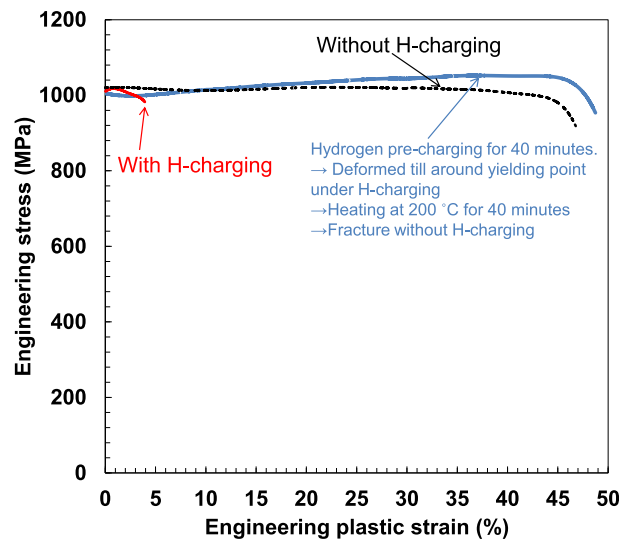


**Fig. 9 – Engineering stress–strain curves of interrupted tests, both, with and without H-charging.**

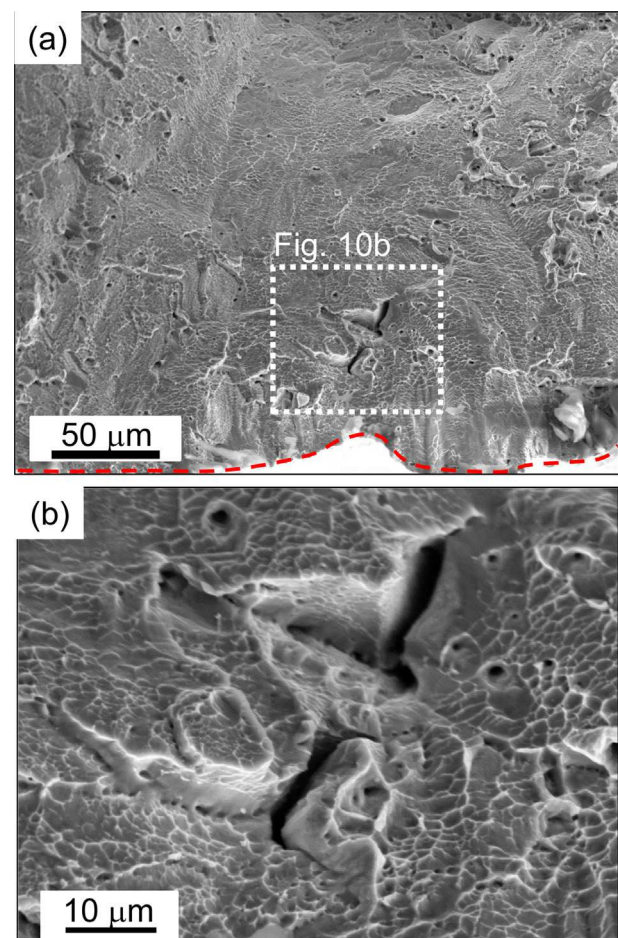


**Fig. 10 – (a) Fractograph of the interrupted tensile test shown in Fig. 9. (b) Magnified image showing grain boundary triple junction cracking in the region indicated by the square in (a).**

**Table 3 – Conventional reports on activation energies for hydrogen desorption from various trap sites.**

Trap site	Steel	Activation energy	Ref
Grain boundary	Pure iron	17 kJ mol <sup>-1</sup>	[28]
Elastic field of edge dislocation	Pure iron Martensitic steel Austenitic steel	27–35 kJ mol <sup>-1</sup>	[28,35,36]
Micro-void	Pure iron	35 kJ mol <sup>-1</sup>	[28]
Σ3 twin boundary	Austenitic steel	62 kJ mol <sup>-1</sup>	[35]
Dislocation core	Martensitic steel	58 kJ mol <sup>-1</sup>	[37,38]
Coherent TiC	Martensitic steel	46–59 kJ mol <sup>-1</sup>	[39]
Semi-coherent TiC	Martensitic steel	56 kJ mol <sup>-1</sup>	[40]
Incoherent TiC	Martensitic steel	68–116 kJ mol <sup>-1</sup>	[39]
Chromium carbide	Austenitic steel	73–96 kJ mol <sup>-1</sup>	[41]

other words, intergranular crack initiation is most probably not caused by slip localization.

Even without hydrogen charging, intergranular cracking was apparently enhanced by slip localization as discussed in Section 4.1 in conjunction with Fig. 5d, although the fracture surface did not reveal brittle features (Fig. 5e). This indicates that slip localization apparently promotes grain boundary cracking by hydrogen-stimulated local ductilization similar to pseudo-embrittlement. Here, the term pseudo-embrittlement refers to the deterioration of the ‘global’ sample ductility through the local promotion of a ductile fracture process [51–53]. Hence, although the local damage is promoted by a highly ductile process, the resulting apparent macroscopic behavior of the sample is brittle. Slip localization in this type of steel is hence enhanced by hydrogen uptake [17] and the associated hydrogen-enhanced localized plasticity (HELP) [51–57] (e.g. material softening due to hydrogen-enhanced dislocation mobility [54]), assisting the ductile fracture along grain boundaries. More specific, we suggest that such confined and hydrogen-enhanced plasticity [54–59] leads to an increased vacancy density which is further stabilized by hydrogen decoration [60,61]. These vacancies can then condensate at the grain boundaries to form hydrogen decorated and hence stable voids which undergo coalescence [62,63]. In fact strain-localization-assisted micro-void formation was observed in the current work in the hydrogen-charged sample (see Figs. 8c and 10b). This hydrogen- and slip-localization-assisted void formation and ensuing ductile fracture effect is apparently related to the ductile fracture features that we observed near the grain boundary as indicated by the circle in Fig. 6d.

The observed hydrogen-assisted cracking phenomena of the investigated Fe–Mn–Al–C  $\kappa$ -precipitation-hardened steel are summarized in the schematics shown in Fig. 12. For the sake of simplicity, Fig. 12 focuses on the cracking mechanism associated with slip localization. As initial step, hydrogen-enhanced slip localization occurs in the sense of the HELP mechanism. The fcc steel matrix with (semi-)coherent precipitates promotes such microbands owing to the reduced dislocation cross slip capability. Such strain localization appears specifically at grain boundaries (see Figs. 5, 8 and 12a). As a result, the grain boundaries are elastically distorted already at an early strain level due to dislocation pile-up, local orientation changes, and formation of steps associated with dislocation–boundary interactions. The simplest case for the latter effect is the interaction between slip dislocation and a Σ3 coherent boundary as described in Refs. [64–66]. Thus, strain localization results also in hydrogen transport into the distorted grain boundaries (Fig. 12b). As discussed above, hydrogen-related cracks first nucleate at grain boundary triple junctions, and the associated slip localization causes void formation as described above (Fig. 12c) creating a preferred crack propagation path along the void-decorated interfaces (Figs. 10b and 12d). Even without micro-void formation, the strain localization along grain boundaries promotes hydrogen-assisted cracking, since the grain boundaries are distorted elastically as well as plastically. The slip-localization-related distortion is assumed to introduce steps on the grain boundaries, resulting in the slip traces observed on the fracture surface shown in Fig. 6d. One should note that hydrogen-assisted slip-localization alone (i.e. with the aid of the HELP effect) does not seem to cause the brittle fracture along grain boundaries, since slip-localization causes fracture

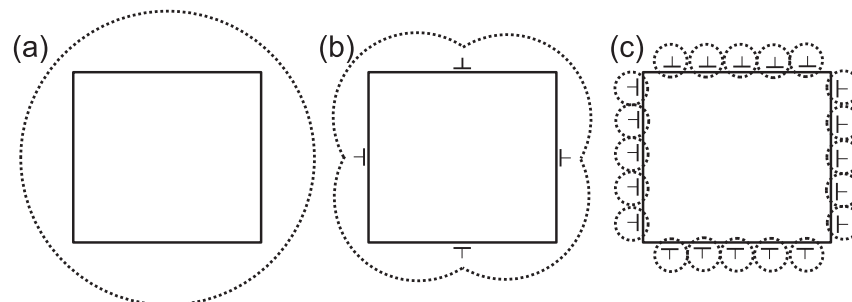


**Fig. 11 – Schematics for correlations among coherency, number of misfit dislocation, and strain field around a precipitate. The introduction of misfit dislocations accommodates the elastic strain field around a precipitate. Squares and dotted lines indicate precipitate and strain field, respectively. (a) Coherent interface without misfit dislocations. (b) Semi-coherent interface with a number of misfit dislocations. (c) Incoherent interface with a considerable amount of misfit dislocations.**

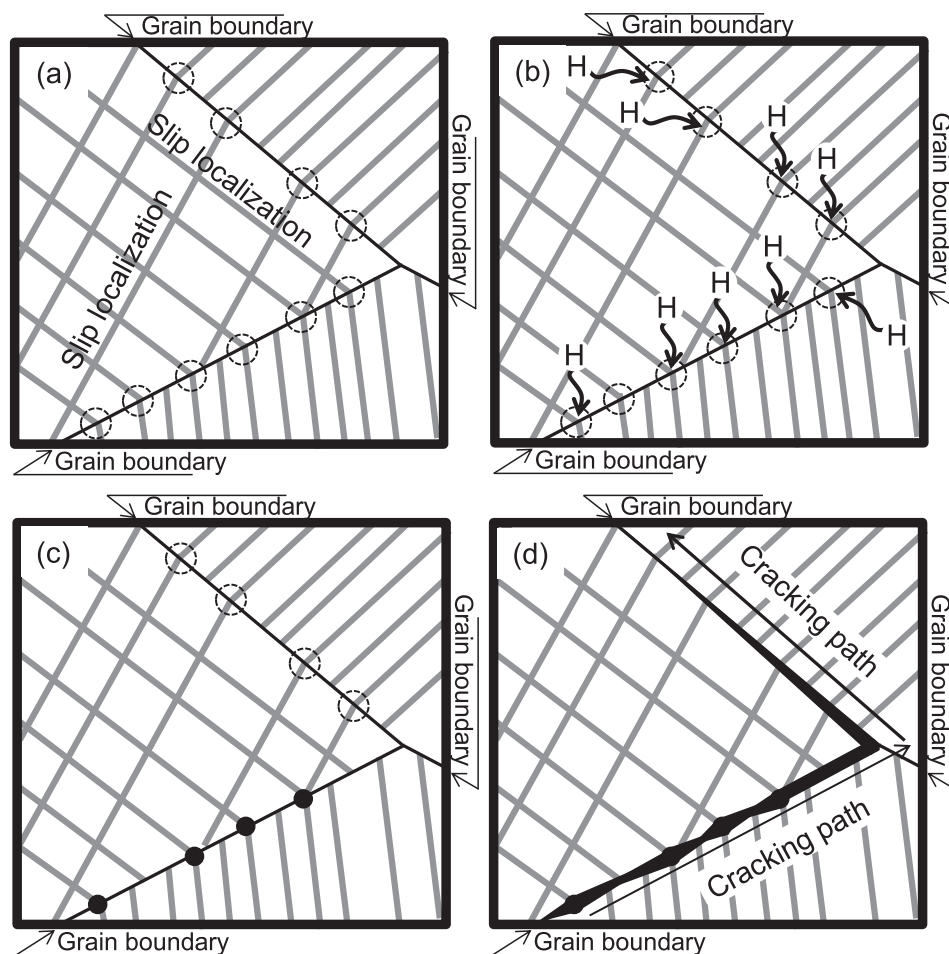


**Fig. 12** – Set of schematical sketches showing the hydrogen-assisted cracking and crack propagation in the present steel. (a) Strain localization occurs particularly on grain boundaries, which is indicated by dotted circles. (b) Diffusible hydrogen moves to the strain-localization regions along the grain boundaries, promoting strain localization through the HELP mechanism. (c) Formation of micro-voids on the grain boundary intersecting strain-localization bands. Micro-voids are indicated by black circles. (d) The micro-voids coalesce and subsequently propagate along the grain boundaries. This strain localization phenomenon, even without the presence of micro-voids, promotes crack propagation through the elastic strain field as well as the hydrogen localization along grain boundaries.

through either cleavage-like or purely ductile mechanisms. An important additional effect in the present context is that the hydrogen uptake reduces both, the grain boundary energy and also its cohesive energy [67–69], enhancing decohesion of the grain boundaries, leading to facilitated hydrogen-assisted intergranular fracture. This means that hydrogen acts not only as a supporting agent for strain localization and accelerated void formation at grain boundaries but has also an immediate effect in reducing grain boundary cohesion.

## 5. Conclusions

Hydrogen effects on the tensile ductility of a  $\kappa$ -carbide-hardened austenitic steel were investigated by tensile testing under ongoing hydrogen charging as well as by thermal desorption analysis. The presence of  $\kappa$ -carbides acts as a hydrogen trap site with an activation energy for hydrogen desorption of approximately  $76\text{--}80\text{ kJ mol}^{-1}$ . Hydrogen embrittlement

occurred through intergranular fracture, caused by two hydrogen-assisted cracking mechanisms: grain boundary triple junction cracking and slip-localization-assisted grain boundary cracking. While the former is a typical hydrogen-assisted cracking mechanism for fcc alloys, the latter appears as a mechanism which is more characteristic of the here investigated Mn–C–Al steel. The slip localization linked to the precipitated  $\kappa$ -carbides causes void formation along grain boundaries, resulting in microscopically ductile intergranular cracking which leads to macroscopic brittle failure. Hydrogen-related cracks seem to first nucleate through grain boundary triple junction cracking, while slip-localization acting on grain boundaries then promotes crack propagation.

## Acknowledgments

M.K. acknowledges the Research Fellowship of the Japan Society for the Promotion of Science for Young Scientists.

## REFERENCES

- [1] Frohberg RP, Barnett WJ, Troiano AR. Delayed failure and hydrogen embrittlement in steel. WADC Tech Rep 1954:54–320.
- [2] Perng TP, Altstetter CJ. Comparison of hydrogen gas embrittlement of austenitic and ferritic stainless steels. *Metall Trans A* 1987;18A:123–34.
- [3] Marchi CS, Somerday BP, Tang X, Schiroky GH. Effects of alloy composition and strain hardening on tensile fracture of hydrogen-precharged type 316 stainless steels. *Int J Hydrogen Energy* 2008;33:889–904.
- [4] Barbier D, Gey N, Allain S, Bozzolo N, Humbert M. Analysis of the tensile behavior of a TWIP steel based on the texture and microstructure evolution. *Mater Sci Eng A* 2009;500:196–206.
- [5] Koyama M, Sawaguchi T, Tsuzaki K. TWIP effect and plastic instability condition in an Fe–Mn–C austenitic steel. *ISIJ Int* 2013;53:323–9.
- [6] Gutierrez-Urrutia I, Raabe D. Dislocation and twin substructure evolution during strain hardening of an Fe–22Mn wt.% Mn–0.6 wt.% C TWIP steel observed by electron channeling contrast imaging. *Acta Mater* 2011;59:6449–62.
- [7] David RS, Jäpel T, Wietbrock B, Eisenlohr P, Gutierrez-Urrutia I, Saeed-Akbari A, et al. Revealing the strain-hardening behavior of twinning-induced plasticity steels: theory, simulations, experiments. *Acta Mater* 2013;61:494–510.
- [8] Koyama M, Sawaguchi T, Lee T, Lee CS, Tsuzaki K. Work hardening associated with  $\epsilon$ -martensitic transformation, deformation twinning, dynamic strain aging in Fe–17Mn–0.6C and Fe–17Mn–0.8C TWIP steels. *Mater Sci Eng A* 2011;528:7310–6.
- [9] Scott C, Allain S, Faral M, Guelton N. The development of a new Fe–Mn–C austenitic steel for automotive applications. *Rev Metal Cah D'inf Tech* 2006;103:293–302.
- [10] De Cooman BC, Chin K-G, Kim J. In: Chiaberge Marcello, editor. High Mn TWIP steels for automotive applications, new trends and developments in automotive system engineering, ISBN 978-953-307-517-4; 2011. InTech.
- [11] Frommeyer G, Brück U. Microstructures and mechanical properties of high-strength Fe–Mn–Al–C light-weight TRIPLEX steels. *Steel Res Int* 2006;77:627–33.
- [12] Springer H, Raabe D. Rapid alloy prototyping: compositional and thermo-mechanical high throughput bulk combinatorial design of structural materials based on the example of 30Mn–1.2C–xAl triplex steels. *Acta Mater* 2012;60:4950–9.
- [13] Seol JB, Raabe D, Choi P, Park HS, Kwak JH, Park CG. Direct evidence for the formation of ordered carbide in a ferrite-based low-density Fe–Mn–Al–C alloy studied by transmission electron microscopy and atom probe tomography. *Scr Mater* 2013;68:348–53.
- [14] Gutierrez-Urrutia I, Raabe D. Influence of Al content and precipitation state on the mechanical behavior of austenitic high Mn low-density steels. *Scr Mater* 2013;68:343–7.
- [15] Choi K, Seo C-H, Lee H, Kim SK, Kwak JH, Chin KG, et al. Effect of aging on the microstructure and deformation behavior of austenite base lightweight Fe–28Mn–9Al–0.8C steel. *Scr Mater* 2010;63:1028–30.
- [16] Gutierrez-Urrutia I, Raabe D. Multistage strain hardening through dislocation substructure and twinning in a high strength and ductile weight-reduced Fe–Mn–Al–C steel. *Acta Mater* 2012;60:5791–802.
- [17] Michler T. Hydrogen environment embrittlement. MPIE work shop on hydrogen embrittlement in steels [cited 2013 June 30]. Available from: [http://www.mpie.de/uploads/media/HES\\_Workshop\\_Michler.pdf](http://www.mpie.de/uploads/media/HES_Workshop_Michler.pdf).
- [18] Michler T, Marchi CS, Nuamann J, Weber S. Hydrogen environment embrittlement of stable austenitic steels. *Int J Hydrogen Energy* 2012;37:16231–46.
- [19] Koyama M, Akiyama E, Tsuzaki K, Raabe D. Hydrogen-assisted failure in a twinning-induced plasticity steel studied under in situ hydrogen charging by electron channeling contrast imaging. *Acta Mater* 2013;61:4607–18.
- [20] Koyama M, Akiyama E, Sawaguchi T, Raabe D, Tsuzaki K. Hydrogen-induced cracking at grain and twin boundaries in an Fe–Mn–C austenitic steel. *Scr Mater* 2012;66:459–62.
- [21] Koyama M, Akiyama E, Tsuzaki T. Effects of static and dynamic strain aging on hydrogen embrittlement in TWIP steels containing Al. *ISIJ Int* 2013;53:1268–74.
- [22] Koyama M, Akiyama E, Tsuzaki K. Hydrogen embrittlement in a Fe–Mn–C ternary twinning-induced plasticity steel. *Corros Sci* 2012;54:1–4.
- [23] Park L-J, Jeong K-H, Jung J-G, Lee CS, Lee Y-K. The mechanism of enhance resistance to the hydrogen delayed fracture in Al-added Fe–18Mn–0.6C twinning-induced plasticity steels. *Int J Hydrogen Energy* 2012;37:9925–32.
- [24] Frankel GS, Latanision RM. Hydrogen transport during deformation in nickel: Part 2. Single crystal nickel. *Metall Trans A* 1986;17A:869–75.
- [25] Tien J, Thompson W, Bernstein IM, Richards RJ. Hydrogen transport by dislocations. *Metall Trans A* 1976;7A:821–9.
- [26] Koyama M, Akiyama E, Tsuzaki K. Hydrogen embrittlement in Al-added twinning-induced plasticity steel by tensile tests during hydrogen charging. *ISIJ Int* 2012;52:2283–7.
- [27] Ryu JH, Kim SK, Lee CS, Suh D-W, Bhadeshia HKDH. Effect of aluminium on hydrogen-induced fracture behaviour in austenitic Fe–Mn–C steel. *Proc R Soc A* 2013;469. <http://dx.doi.org/10.1098/rspa.2012.0458>.
- [28] Choo WY, Lee JY. Thermal analysis of trapped hydrogen in pure iron. *Metall Trans A* 1982;13A:135–40.
- [29] Koyama M, Akiyama E, Tsuzaki K. Effect of hydrogen content on the embrittlement in a Fe–Mn–C twinning-induced plasticity steel. *Corros Sci* 2012;59:277–81.
- [30] Gutierrez-Urrutia I, Zaefferer S, Raabe D. Electron channeling contrast imaging of twins and dislocations in twinning-induced plasticity steels under controlled diffraction conditions in scanning electron microscope. *Scr Mater* 2009;61:737–40.
- [31] Brewer LN, Field DP, Merriman CC. Mapping and assessing plastic deformation using EBSD. In: Schwartz AJ, Kumar M, Adams BL, Field DP, editors. *Electron backscatter diffraction in material science*. New York: Springer Science+Business Media; 2000.
- [32] Sato K, Tagawa K, Inoue Y. Spinodal decomposition and mechanical properties of an austenitic Fe–30wt.%Mn–9wt.%Al–0.9wt.%C alloy. *Mater Sci Eng A* 1989;A111:45–50.
- [33] Choo WK, Kim JH, Yoon JC. Microstructural change in austenitic Fe–30.0wt%Mn7.8wt%Al–1.3wt%C initiated by spinodal decomposition and its influence on mechanical properties. *Acta Mater* 1997;45:4877–85.
- [34] Wang CS, Hwang CN, Chao CG, Liu TF. Phase transitions in an Fe–9Al–30Mn–2.0C alloy. *Scr Mater* 2007;57:809–12.
- [35] So KH, Kim JS, Chun YS, Park K-T, Lee Y-K, Lee CS. Hydrogen delayed fracture properties and internal hydrogen behavior of a Fe–18Mn–1.5Al–0.6C TWIP steel. *ISIJ Int* 2009;49:1952–9.
- [36] Frappart S, Oudriss A, Feaugas X, Creus J, Bouhattate J, Thébault F, et al. Hydrogen trapping in martensitic steel investigated using electrochemical permeation and thermal desorption spectroscopy. *Scr Mater* 2011;65:859–62.
- [37] Thomas RLS, Li D, Gangloff RP, Scully JR. Trap-governed hydrogen diffusivity and uptake capacity in ultrahigh-strength AERMET 100 steel. *Metall Mater Trans A* 2002;33A:1991–2004.
- [38] Frappart S, Feaugas X, Creus J, Thébault F, Delattre, Marchebois H. Study of the hydrogen diffusion and

- segregation into Fe–C–Mo martensitic HSLA steel using electrochemical permeation test. *J Phys Chem Solids* 2010;71:1467–79.
- [39] Wei FG, Hara T, Tsuzaki K. Precise determination of the activation energy for desorption of hydrogen in two Ti-added steels by a single thermal-desorption spectrum. *Metall Mater Trans B* 2004;35B:587–97.
- [40] Wei FG, Tsuzaki K. Quantitative analysis on hydrogen trapping of TiC particles in steel. *Metall Mater Trans A* 2006;37A:331–53.
- [41] Mizuno M, Anzai H, Aoyama T, Suzuki T. Determination of hydrogen concentration in austenitic stainless steels by thermal desorption spectroscopy. *Mater Trans JIM* 1994;35:703–7.
- [42] Taketomi S, Matsumoto R, Miyazaki N. Atomistic study of hydrogen distribution and diffusion around a {112}<111> edge dislocation in alpha iron. *Acta Mater* 2008;56:3761–9.
- [43] Martin ML, Somerday BP, Ritchie RO, Sofronis P, Robertson IM. Hydrogen-induced intergranular failure in nickel revisited. *Acta Mater* 2012;60:2739–45.
- [44] Fukushima H, Birnbaum HK. Surface and grain boundary segregation of deuterium in nickel. *Acta Metall* 1984;32:851–9.
- [45] Ladna B, Birnbaum HK. SIMS study of hydrogen at the surface and grain boundaries of nickel bicrystals. *Acta Metall* 1987;35:2537–42.
- [46] Schober T, Dieker C. Observation of local hydrogen on nickel surface. *Metall Trans A* 1983;14A:2440–2.
- [47] Ovejero-Garcia J. Hydrogen microprint technique in the study of hydrogen in steels. *J Mater Sci* 1985;20:2623–9.
- [48] Li D, Gangloff RP, Scully JR. Hydrogen trap states in ultrahigh-strength AERMET 100 steel. *Metall Mater Trans A* 2004;35A:849–64.
- [49] Takai K, Watanuki R. Hydrogen in trapping states innocuous to environmental degradation of high-strength steels. *ISIJ Int* 2003;43:520–6.
- [50] Wilcox BA, Smith GC. Intercrystalline fracture in hydrogen-charged nickel. *Acta Metall* 1965;13:331–43.
- [51] Wang S, Hashimoto N, Wang Y, Ohnuki S. Activation volume and density of mobile dislocations in hydrogen-charged iron. *Acta Mater* 2013;61:4734–42.
- [52] Barnoush A, Vehoff H. Recent developments in the study of hydrogen embrittlement: hydrogen effect on dislocation nucleation. *Acta Mater* 2010;58:5274–85.
- [53] Sofronis P, Lianga Y, Aravas N. Hydrogen induced shear localization of the plastic flow in metals and alloys. *Eur J Mech A – Solid* 2001;20:857–72.
- [54] Birnbaum HK, Sofronis P. Hydrogen-enhanced localized plasticity—a mechanism for hydrogen-related fracture. *Mater Sci Eng A* 1994;176:191–202.
- [55] Robertson IM, Birnbaum HK. An HVEM study of hydrogen effects on the deformation and fracture of nickel. *Acta Metall* 1986;34:353–66.
- [56] von Pezold J, Lymperakis L, Neugebauer J. Hydrogen-enhanced local plasticity at dilute bulk H concentrations: the role of H–H interactions and the formation of local hydrides. *Acta Mater* 2011;59:2969–80.
- [57] Maxelon JM, Pundt A, Pyckhout-Hintzen W, Barker J, Kirchheim R. Interaction of hydrogen and deuterium with dislocations in palladium as observed by small angle neutron scattering. *Acta Mater* 2001;49:2625–34.
- [58] Neeraj T, Srinivasan R, Li J. Hydrogen embrittlement of ferritic steels: observations on deformation microstructure, nanoscale dimple and failure by nanovoiding. *Acta Mater* 2012;60:5160–71.
- [59] Barnoush A, Vehoff H. Electrochemical nanoindentation: a new approach to probe hydrogen/deformation interaction. *Scr Mater* 2006;55:195–8.
- [60] Nagumo M. Function of hydrogen in embrittlement of high-strength steels. *ISIJ Int* 2001;41:590–8.
- [61] Nagumo M. Hydrogen related failure of steels – a new aspect. *Mater Sci Technol* 2004;20:940–50.
- [62] Ahn DC, Sofronis P, Dodds Jr RH. On the hydrogen-induced plastic flow localization during void growth and coalescence. *Int J Hydrogen Energy* 2007;32:3734–42.
- [63] Liang Y, Ahn DC, Sofronis P, Dodds Jr RH, Bammann D. Effect of hydrogen trapping on void growth and coalescence in metals and alloys. *Mech Mater* 2008;40:115–32.
- [64] Mahajan S, Chin GY. Twin-slip, twin-twin and slip-twin interactions in Co–8wt.% Fe alloy single crystals. *Acta Metall* 1973;21:173–9.
- [65] Remy L. Twin-slip interaction in f.c.c. crystals. *Acta Metall* 1977;25:711–4.
- [66] Wang YB, Sui ML. Atomic-scale in situ observation of lattice dislocations passing through twin boundaries. *Appl Phys Lett* 2009;94:021909.
- [67] Oriani RA. Hydrogen embrittlement of steels. *Ann Rev Mater Sci* 1978;8:327–57.
- [68] Kirchheim R. Reducing grain boundary, dislocation line and vacancy formation energies by solute segregation: II. Experimental evidence and consequence. *Acta Mater* 2007;55:5139–48.
- [69] Yamaguchi M, Ebihara K, Itakura M, Kadoyoshi T, Suzudo T, Kaburaki H. First-principles study on the grain boundary embrittlement of metals by solute segregation: part II. Metal (Fe, Al, Cu)-hydrogen (H systems). *Metall Mater Trans A* 2011;42A:330–9.